Regular Article

Energy and angular distribution of electrons ejected from water by the impact of fast O^{8+} ion beams

Shamik Bhattacharjee[1], Chandan Bagdia[1], Madhusree Roy Chowdhury[1], Juan M. Monti[2], Roberto D. Rivarola[2], and Lokesh C. Tribedi[1,a]

[1] Tata Institute of Fundamental Research, Homi Bhabha Road, Coloba, Mumbai 400005, India
[2] Institute de Fisica Rosario (CONICET-UNR), Universidad Nacional de Rosario, 2000 Rosario, Argentina

Abstract. Double differential cross sections (DDCS) of electrons emitted from vapor water molecules (in vapor phase) by 2.0 MeV/u and 3.75 MeV/u bare oxygen ion impact have been measured by continuum electron spectroscopy technique. The ejected electrons were detected by an electrostatic hemispherical deflection analyzer over an energy range of 1–600 eV and emission angles from $20°$ to $160°$. The DDCS data has been compared with the continuum-distorted-wave-eikonal-initial state (CDW-EIS) approximation and a reasonable agreement was found with both version of the models i.e. post and prior version. By numerical integration of the DDCS data, the single differential cross section (SDCS) and total ionization cross section (TCS) were obtained. The obtained TCS results were compared with other available TCS results for water target within the same energy range. The total ionization cross sections values are seen to saturate as the projectile charge state (q_p) increases, which is in contrast to the first-Born predicted q_p^2 dependence. This is also in contrast to the prediction of the CDW-EIS models.

1 Introduction

Energy loss curve of high-velocity ions has a sharp maximum at the end of their trajectories, which is commonly known as the Bragg peak. This fact makes ion beam radiation therapy one of the most useful techniques for treating cancer [1,2]. In radiation therapy, high-velocity ions are directed toward the infected cells. For high-velocity ion beams, most of the energy loss is due to ionization of the target. Ionization of target cells produce a lot of secondary electrons in all directions. The low energy electrons may induce single or double strand breaks of DNAs or RNAs of cancer cells [3,4]. Hence the study of energy and angular distribution of the secondary electrons is especially important in order to understand radiation damage caused by the energetic ion beams [5].

In the case of hadron therapy in human body, most of the energy is deposited in ionizing the water molecules since 60% of the body weight comprises of water. It thus appears crucial to obtain accurate differential and total ionization cross sections for water molecule, for the modeling of radiation therapy in the human body [6,7]. The protons and also C-ions are most commonly used for treating cancer patients worldwide. Although the current measurements were done for water vapor target, it should be mentioned that in actual cases, water is present in liquid phase, and not in gas phase. The most important difference between gas and condensed phase is the transport

and cascade multiplication of secondary electrons. This has been addressed in the literature by different groups [8–11]. Also, the phase effects in stopping around and below the maximum of energy loss have been demonstrated by the Linz group [12,13]. However, the data for vapor phase will be still useful input to calculate that for liquid phase. In absence of the experimental data on liquid water one may find that the existing data for water vapor can be of useful input for the radiation damage modeling.

The database for cross section data for electron emission from water target by the impact of highly charged projectiles is scarce. Although in recent years cross section measurement of biologically relevant targets, including water, have attracted increasing attention because of its importance in radiation biology or radiation therapy. For example, the references [14–18] deal with the ionization of DNA or RNA base molecules whereas the DDCS or TCS data on the ionization of water has been presented in [19–24].

In this work, we present the absolute double differential ionization cross section of e^- ejected from vapor phase water molecules by 2.0 MeV/u and 3.75 MeV/u bare oxygen ion impact. This work is a continuation of our previous work, where we have initiated the study of ionization of water molecules by the impact of C^{6+}, O^{8+} and Si^{13+} ions. Apart from presenting the DDCS data for the C and O beams at above energies, we also present here all the available TCS data for the different projectiles and charge states. The TCS data were plotted together as a function of the charge states in order to

[a] e-mail: lokesh@tifr.res.in

check the so called saturation behavior arising from higher order scattering mechanisms (see below).

In this work, the experimentally measured double differential cross section, single differential cross section (SDCS) and the total ionization cross section (TCS) were compared with the CDW-EIS [25,26] model calculations for bare oxygen ions impacting on H_2O molecule. The CDW-EIS model has been widely used in describing the single electron ionization at intermediate and high energy range. This model represents the first order term of a distorted wave series by including the distortions due to the long-range Coulomb potential in both the initial and final channels. In this way, it was then possible to account for two center effects, which were not included in first Born or plane wave approximations.

In the CDW-EIS model, the electron to be ionized is described in the entry channel by a two-center wavefunction, given by the product of a target bound orbital and a projectile continuum eikonal phase, while in the exit channel the ionized electron is described also by a two-center wavefunction given by a product of a plane wave and two continuum factors, one associated with the residual target field and the other one with the projectile field. During the collision, the non-ionized electrons are considered to remain as frozen in their initial orbitals. The differences between the prior and post versions of the model could be attributed to the importance of the correlation between the active (ionized) and passive (non-ionized) electrons. The prior version includes in its description the influence of the passive electrons on the dynamical evolution of the ejected one (the so called dynamical screening) [27], whereas in the post-version it is only partially taken into account through the use of an effective charge.

In Section 2, we briefly describe the experimental setup used to measure the double differential cross section of ejected secondary electrons for the current collision system. In Section 3, we discussed about the DDCS deduction method and also about the estimation of various sources of errors. In Section 4, we present the experimental results along with a detailed comparison with theoretical models. In the last section (Sect. 5), we have shown the dependence of the scaled total ionization cross section (TCS $\times E/\ln E$, E being the projectile energy in a.u.), on the projectile charge state (q_p).

2 Experimental setup

Highly charged oxygen beams of energy $2.0\,\mathrm{MeV/u}$ and $3.75\,\mathrm{MeV/u}$ were generated from the BARC-TIFR pelletron accelerator facility situated at TIFR, Mumbai. After final energy selection, the O^{q+} ions were passed through a post acceleration foil stripper. This was used to produce bare oxygen ions. These ions were then selected by a switching magnet. Before entering the chamber, the beam was tightly collimated to a size of about $1.5 \times 1.5\,\mathrm{mm^2}$ by the help of two sets of 4-jaw slits kept a meter away from each other. The 4-jaw slits are motor controlled remotely.

The interaction chamber was kept at a base pressure of 2×10^{-7} mbar. Two μ-metal sheets having high magnetic

permeability was placed inside the chamber along its perimeter to reduce the earth's magnetic field inside the chamber. This was essential for the detection of low energy electrons. For analyzing secondary electron energies, we have used a hemispherical electrostatic deflection analyzer. This analyzer was kept on a rotatable turntable inside the chamber. The inner and outer electrodes of the hemispherical analyzer were made of oxygen-free high conductivity (OFHC) copper. In order to avoid generation of secondary electrons from the analyzer electrodes, the inner surfaces of the electrodes were coated with carbon soot. The analyzer energy resolution depends mostly on the exit slit width and the acceptance angle of the entrance slit and for the present analyzer, it is about 5–6% of electron energy. The accuracy of the angular distributions for this spectrometer has been tested by reproducing the expected angular distribution in case of elastic scattering of electrons from Ar atoms which was done earlier (see Ref. [28]), and again reproduced recently during this work.

The energy analyzed electrons were detected by a channel electron multiplier. The front side of the channeltron was kept at a potential of 100 V to maintain uniform detection efficiency for the electrons. The entire chamber was filled with water vapor at a pressure of 0.15 mTorr. During data collection, the outer walls of the scattering chamber were heated at ≈50 °C. The heating was done to reduce the sticking of water molecules on the chamber wall which finally reduced the overall background counts.

3 Deduction of the DDCS

If a beam of N_p ions enters the water vapor target, and as a result N_e number of electrons having energy ϵ are ejected into a solid angle Ω, then the DDCS values for electron emission are obtained from the following equation,

$$\frac{d^2\sigma}{d\Omega_e d\epsilon_e} = \frac{N_e/N_{pe} - N_b/N_{pb}}{n\epsilon_{el}(l\Omega)_{eff}\Delta\epsilon} \qquad (1)$$

where N_e and N_b are the number of total and background counts respectively, whereas N_{pe} and N_{pb} are the number of projectile ions in presence and absence of target gas respectively. The counts N_e, for low energy electrons, were modified to take into account the electrons lost due to scattering before reaching the detector. In such cases N_e was replaced by $N_e/\exp(-nl\sigma_{sc})$ where $n =$ gas density, $l =$ distance traveled by electrons before reaching the analyzer. The corrections are found important only for electron energies around 1–7 eV, The total scattering cross section can be found in [29,30]). This correction (using [29]) was approximately 18% at 1 eV and reduced to about 5% at 5 eV and negligible above 8 eV. The quantity $\Delta\epsilon$ is the energy resolution of the spectrometer, which is 5–6% of the electron energy [28]. The detection efficiency of the channeltron detector (ϵ_{el}) is ≈90%. The parameter n is the water-vapor target density inside the chamber and $(l\Omega)_{eff}$ is the solid angle path length. For details about the measurement technique, one may refer to [28].
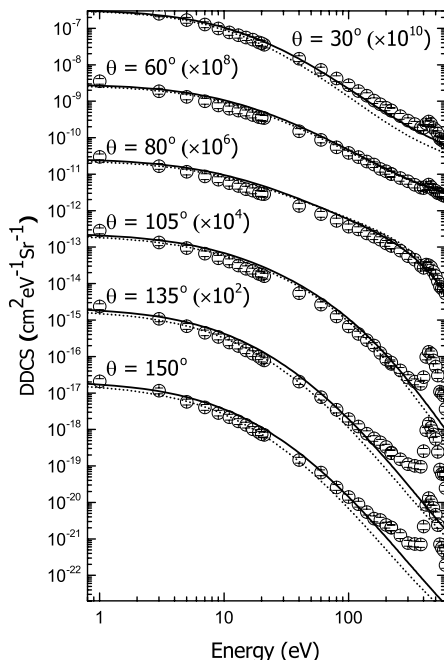
Fig. 1. Double differential cross sections of secondary electrons (1–600 eV) for 2.0 MeV/u O^{8+} projectile. The experimental results have been represented by the circles (∘). The CDW-EIS prior version is represented by the solid lines, while the post version has been represented by the dotted line. For convenience, both theory and data are multiplied by suitable factors as shown in figure.

The measurements were carried out over an angular range of 20–160° for both 2 MeV/u and 3.75 MeV/u O^{8+} ions. For each angle, the number of electrons having energies in the range of 1–600 eV were scanned. The SDCS values were obtained from the measured DDCS by numerical integration with respect to the ejected angle or energy. In the process of numerical integration, DDCS values for angles from 0° to 20° and 160° to 180° were extrapolated by polynomial fitting technique.

Good statistics was maintained during the experiment. The statistical error was obtained from the net electron counts ($N_e - N_b$). For both 3.75 MeV/u and 2.0 MeV/u projectiles, the statistical error was less than 5%. Error in the measurement of water-vapor density n (±10%), spectrometer resolution Δ (±5%) and the solid angle path length $(l\Omega)_{eff}$ (±5%) were the other sources of error. Overall the total experimental error was not more than 18–20%.

4 Experimental results

The scope of the present work was to compare the experimental double differential, single differential and total ionization cross sections with those predicted by the CDW-EIS model calculations for water vapor ionization with 2.0 MeV/u and 3.75 MeV/u O^{8+} projectiles. The present set of TCS data were compared with some of our previous data for C^{6+}, O^{8+} and Si^{13+} projectiles.
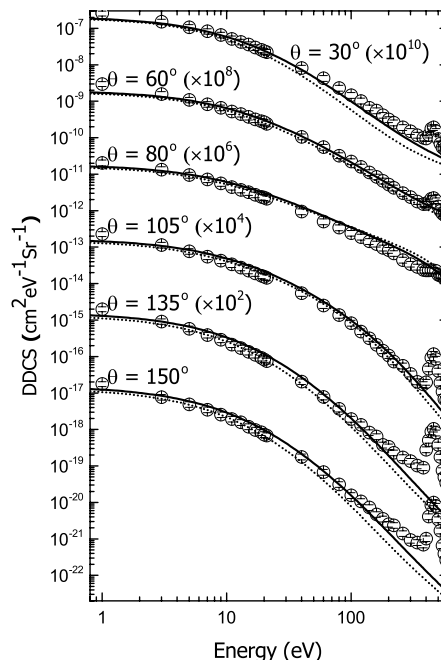
Fig. 2. Same as in Figure 1, but for 3.75 MeV/u O^{8+} projectile.

The comparison was also done for other projectiles in the similar velocity range, such as H^+, He^+, He^{++} and C^{6+}.
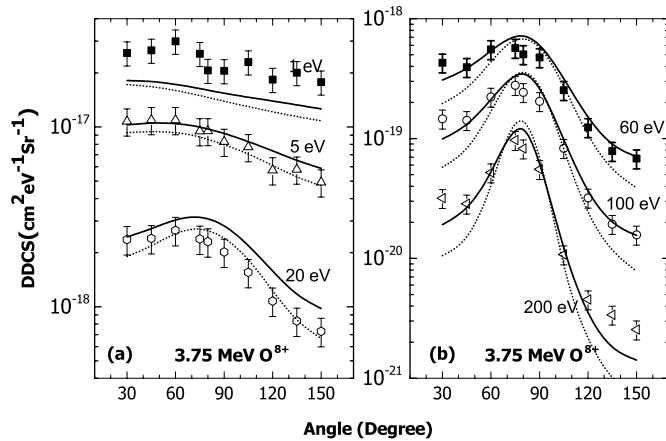
4.1 DDCS energy distribution

Figures 1 and 2 show the DDCS energy distribution of electrons emitted from water-vapor in collisions with 2.0 MeV/u and 3.75 MeV/u O^{8+} projectiles respectively. All the spectra show a monotonic decrease in electron counts with increasing electron energy. The peaks near 500 eV on all the spectra are due to the KLL Auger electron emission from 1s vacancies in the oxygen atom. The low energy part of each spectrum is attributed to the soft collision electrons, i.e. electrons which are ionized because of high impact parameter collisions. In the medium energy region, electron dynamics is governed by both the target and projectile centers. This region is typically known as two center electron emission (TCEE) for an atomic target. However, for a molecule like H_2O, such a definition of target center may not be as simple as atomic one. Comparison of the experimental results with the CDW-EIS model calculations show good agreement for almost all the emission angles, although a better agreement can be seen for forward angles than for backward angles. Excellent agreement can be seen near the angles $\theta = 80$–90°.

4.2 DDCS angular distribution

Figures 3 and 4 display the angular distributions of ejected electrons as a function of ejection angle for the case of 2.0 MeV/u and 3.75 MeV/u projectiles, respectively. The angular distributions are plotted for six different electron energies, ranging from 1 eV to 200 eV. It can be seen from both the plots that as the ejected electron energy increases, the peak around 70° becomes sharper which
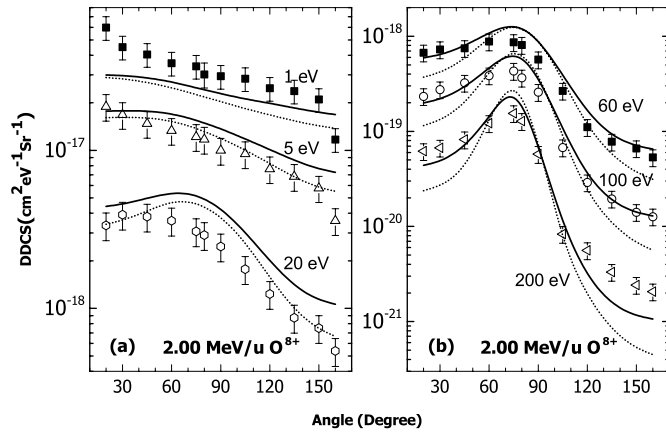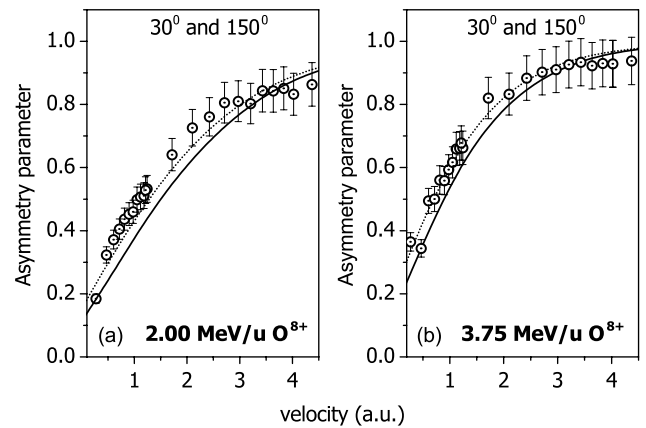
Fig. 3. DDCS angular distribution plots for six different electron energies for 2.0 MeV/u projectile. In each plot the solid line represents the CDW-EIS prior version model while the dotted line represents its post version.
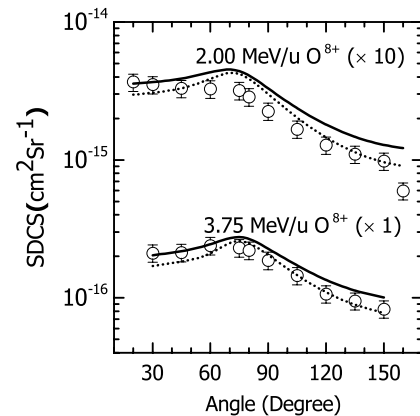

Fig. 5. The asymmetry parameter for 2.0 MeV/u (a) and 3.75 MeV/u (b) versus ejected electron velocity. The CDW-EIS prior version is represented by the solid lines, while the post version has been represented by the dotted line.

Fig. 4. Same as in Figure 3, but for 3.75 MeV/u projectile.

Fig. 6. Single differential cross sections for ejection of electrons by 2.0 MeV/u and 3.75 MeV/u O^{8+} ions in collision with waver vapor as a function of the ejected electron angle. The CDW-EIS prior version is shown by the solid line whereas the dotted line represents the CDW-EIS post version. Experimental measurements are represented by circles ($\circ$). For convenience, data and theoretical values for the case of 2.0 MeV/u O^{8+} has been multiplied by a suitable factor as indicated in the figure.

is well known due to binary collision effect in ion–atom collision. However, at lowest energies, such as 1 eV and 5 eV one observes gradual fall of DDCS going from forward to backward angles (which is more evident in Fig. 4). This behavior is in contrast to the generally observed flat-distribution in fast-ion collisions with many-electron atoms like Ne (or 2-electron atom like He) collisions for such low energy electrons. For example, one may refer reference [31] (e.g. see Fig. 6 in this reference). The observed steep fall in angular distribution, was seen even up to 20 eV or so. This behavior could be related to the molecular behavior of water and well reproduced by the CDW-EIS models. The difference between forward and backward angles, for the low energy electrons, can be quantified in terms of forward–backward asymmetry and is discussed in next section.

For 2.0 MeV/u ions (Fig. 3), comparison of the experimental results with the theoretical calculations show reasonably good agreement with both the prior and post versions of the CDW-EIS model, though the post version matches better with experimental results for low energies, e.g. at 5 eV and 20 eV (Fig. 3a). At higher

energies e.g. for 100 eV and 200 eV, the deviation with the post-version model is increase more for large angles, and comparatively less for angles near 90°, though a contrasting behavior is observed for some low energy regions. The 3.75 MeV/u projectile plots (Fig. 4) also show similar behavior, though matching with the theory is better for the case of 2.0 MeV/u projectile.

4.3 Forward–backward asymmetry parameter

In Figures 3 and 4, we have noticed a substantial difference between the DDCS values for extreme forward and backward angles. This forward–backward asymmetry in electron emission cross section, at least in case of ion–atom ionization, arises because of the well known TCEE and the post-collision interaction (PCI), where the ionized electron trajectory is governed by both the projectile and

Table 1. DDCS, SDCS and TCS values for the case of $2\,\mathrm{MeV/u}$ O^{8+} projectile (DDCS unit – $\mathrm{cm^2\,eV^{-1}\,Sr^{-1}}$).

E	30°	45°	60°	75°	80°	90°	105°	120°	135°	150°	$d\sigma/d\epsilon$
1	4.5E−17	4.0E−17	3.6E−17	3.4E−17	3.0E−17	2.9E−17	2.8E−17	2.5E−17	2.4E−17	2.1E−17	3.6E−16
3	2.5E−17	2.1E−17	1.9E−17	1.8E−17	1.7E−17	1.5E−17	1.3E−17	1.2E−17	1.1E−17	1.2E−17	1.9E−16
5	1.7E−17	1.5E−17	1.3E−17	1.2E−17	1.2E−17	1.0E−17	9.5E−18	7.6E−18	6.8E−18	5.8E−18	1.3E−16
7	1.3E−17	1.1E−17	1.0E−17	9.6E−18	8.7E−18	7.4E−18	6.7E−18	5.4E−18	4.5E−18	4.1E−18	9.2E−17
9	1.0E−17	8.9E−18	7.7E−18	7.7E−18	7.2E−18	5.8E−18	5.0E−18	4.2E−18	3.5E−18	2.9E−18	7.2E−17
11	7.8E−18	7.1E−18	6.3E−18	6.2E−18	5.8E−18	4.9E−18	4.0E−18	3.2E−18	2.4E−18	2.2E−18	5.7E−17
13	6.6E−18	6.2E−18	5.6E−18	5.1E−18	4.8E−18	3.9E−18	3.2E−18	2.5E−18	2.0E−18	1.7E−18	4.8E−17
15	5.7E−18	5.2E−18	4.9E−18	4.5E−18	3.9E−18	3.3E−18	2.6E−18	1.9E−18	1.5E−18	1.3E−18	4.0E−17
17	4.9E−18	4.4E−18	4.3E−18	4.1E−18	3.6E−18	3.2E−18	2.2E−18	1.6E−18	1.2E−18	1.0E−18	3.5E−17
19	4.1E−18	4.0E−18	3.7E−18	3.4E−18	3.0E−18	2.6E−18	1.9E−18	1.3E−18	1.0E−18	8.4E−19	3.0E−17
20	3.9E−18	3.8E−18	3.6E−18	3.1E−18	2.9E−18	2.5E−18	1.8E−18	1.2E−18	8.7E−19	7.5E−19	2.8E−17
40	1.5E−18	1.5E−18	1.5E−18	1.5E−18	1.4E−18	9.8E−19	5.5E−19	3.0E−19	2.1E−19	1.5E−19	1.1E−17
60	7.2E−19	7.5E−19	8.8E−19	8.6E−19	8.1E−19	5.7E−19	2.7E−19	1.1E−19	7.8E−20	6.6E−20	5.8E−18
80	4.2E−19	4.8E−19	5.5E−19	6.0E−19	5.3E−19	3.8E−19	1.3E−19	5.3E−20	3.5E−20	2.6E−20	3.6E−18
100	2.8E−19	3.2E−19	3.9E−19	4.3E−19	3.7E−19	2.6E−19	6.8E−20	2.9E−20	2.0E−20	1.4E−20	2.4E−18
140	1.4E−19	1.7E−19	2.2E−19	2.7E−19	2.4E−19	1.4E−19	2.8E−20	1.3E−20	7.7E−21	5.5E−21	1.4E−18
180	8.3E−20	9.9E−20	1.4E−19	1.9E−19	1.6E−19	7.7E−20	1.3E−20	6.6E−21	4.5E−21	3.3E−21	8.6E−19
220	5.5E−20	6.9E−20	1.0E−19	1.4E−19	1.1E−19	4.2E−20	6.3E−21	4.0E−21	2.3E−21	2.0E−21	5.9E−19
260	3.9E−20	4.3E−20	7.9E−20	9.7E−20	8.1E−20	2.5E−20	4.2E−21	2.2E−21	1.5E−21	1.3E−21	4.1E−19
300	3.0E−20	3.4E−20	6.4E−20	7.6E−20	5.7E−20	1.5E−20	2.7E−21	1.3E−21	1.1E−21	7.7E−22	3.1E−19
$d\sigma/d\Omega$	3.5E−16	3.3E−16	3.3E−16	3.2E−16	2.9E−16	2.3E−16	1.7E−16	1.3E−16	1.1E−16	9.8E−17	2.9E−15 (TCS)

Table 2. Same as in Table 1, but for $3.75\,\mathrm{MeV/u}$ O^{8+} projectile (DDCS unit – $\mathrm{cm^2\,eV^{-1}\,Sr^{-1}}$).

E	30°	45°	60°	75°	80°	90°	105°	120°	135°	150°	$d\sigma/d\epsilon$
1	2.6E−17	2.7E−17	3.0E−17	2.6E−17	2.1E−17	2.1E−17	2.3E−17	1.8E−17	2.0E−17	1.8E−17	2.5E−16
3	1.5E−17	1.5E−17	1.6E−17	1.4E−17	1.3E−17	1.2E−17	1.2E−17	8.4E−18	9.2E−18	7.8E−18	1.3E−16
5	1.1E−17	1.1E−17	1.1E−17	9.5E−18	9.5E−18	8.3E−18	7.7E−18	5.7E−18	5.8E−18	4.9E−18	9.1E−17
7	8.3E−18	8.1E−18	8.3E−18	7.2E−18	7.2E−18	6.1E−18	5.5E−18	4.4E−18	3.9E−18	3.5E−18	6.7E−17
9	6.6E−18	6.5E−18	6.7E−18	5.8E−18	5.7E−18	5.0E−18	4.3E−18	3.4E−18	2.9E−18	2.6E−18	5.3E−17
11	5.2E−18	5.0E−18	5.3E−18	4.6E−18	4.5E−18	4.0E−18	3.4E−18	2.6E−18	2.2E−18	2.0E−18	4.2E−17
13	4.3E−18	4.1E−18	4.5E−18	3.9E−18	3.8E−18	3.3E−18	2.8E−18	2.2E−18	1.7E−18	1.6E−18	3.5E−17
15	3.6E−18	3.5E−18	3.7E−18	3.3E−18	3.2E−18	2.9E−18	2.3E−18	1.7E−18	1.4E−18	1.2E−18	2.9E−17
17	3.0E−18	3.0E−18	3.2E−18	2.8E−18	2.7E−18	2.5E−18	1.9E−18	1.4E−18	1.1E−18	9.8E−19	2.5E−17
19	2.6E−18	2.6E−18	2.8E−18	2.6E−18	2.4E−18	2.2E−18	1.7E−18	1.2E−18	9.2E−19	8.4E−19	2.2E−17
20	2.4E−18	2.4E−18	2.7E−18	2.4E−18	2.3E−18	2.0E−18	1.6E−18	1.1E−18	8.3E−19	7.3E−19	2.0E−17
40	8.2E−19	8.6E−19	1.1E−18	1.0E−18	9.5E−19	8.2E−19	5.5E−19	3.2E−19	2.1E−19	1.8E−19	7.5E−18
60	4.3E−19	3.9E−19	5.5E−19	5.7E−19	5.0E−19	4.8E−19	2.5E−19	1.2E−19	7.9E−20	6.8E−20	3.8E−18
80	2.3E−19	2.3E−19	3.3E−19	3.7E−19	3.5E−19	3.0E−19	1.4E−19	6.0E−20	3.7E−20	3.1E−20	2.3E−18
100	1.5E−19	1.4E−19	2.2E−19	2.8E−19	2.4E−19	2.0E−19	8.3E−20	3.2E−20	1.9E−20	1.6E−20	1.5E−18
140	6.7E−20	7.0E−20	1.1E−19	1.6E−19	1.5E−19	1.1E−19	3.2E−20	1.2E−20	8.3E−21	7.3E−21	7.9E−19
180	4.2E−20	4.0E−20	6.6E−20	1.2E−19	9.6E−20	7.1E−20	1.5E−20	5.6E−21	3.8E−21	3.6E−21	5.0E−19
220	2.6E−20	2.6E−20	4.2E−20	7.7E−20	6.8E−20	4.6E−20	7.3E−21	3.6E−21	2.3E−21	2.4E−21	3.2E−19
260	1.9E−20	2.8E−20	3.0E−20	6.0E−20	8.9E−20	4.8E−20	5.6E−21	1.5E−20	1.7E−21	1.4E−21	3.2E−19
300	1.5E−20	2.0E−20	2.4E−20	4.9E−20	6.9E−20	3.5E−20	3.4E−21	1.2E−20	1.4E−21	9.3E−22	2.4E−19
$d\sigma/d\Omega$	2.1E−16	2.1E−16	2.4E−16	2.3E−16	2.2E−16	1.9E−16	1.5E−16	1.1E−16	9.5E−17	8.3E−17	2.1E−15 (TCS)

target centers. In case of two- or multi-electron atoms, besides the TCEE and PCI mechanisms, the screened Coulomb or non-Coulomb potential can also introduce such forward–backward asymmetry [32]. In order to quantify this angular asymmetry, we have calculated and plotted a single parameter i.e. the forward–backward asymmetry parameter $\alpha(v_e, \theta)$, defined as,

$$\alpha(v_e\theta) = \frac{\sigma(v_e, \theta) - \sigma(v_e, \pi - \theta)}{\sigma(v_e, \theta) + \sigma(v_e, \pi - \theta)} \quad (2)$$

Here $\sigma(v_e, \theta)$ and $\sigma(v_e, \pi - \theta)$ represent the DDCS values for a forward angle θ and the corresponding complementary (backward) angle $(\pi - \theta)$, respectively. Figure 5 shows the asymmetry parameter $[\alpha(v_e, \theta)]$ as a function of ejected electron velocity (v_e, in a.u.) deduced from the DDCS measured at angles 30° and 150°. The plots for both the projectiles show sharp rise in asymmetry parameter as electron velocity increases. For very low energy electrons, e.g. for $v_e \sim 0.5$ a.u, the value is around 0.35 (in Figs. 5a and 5b). This value at such low energy is
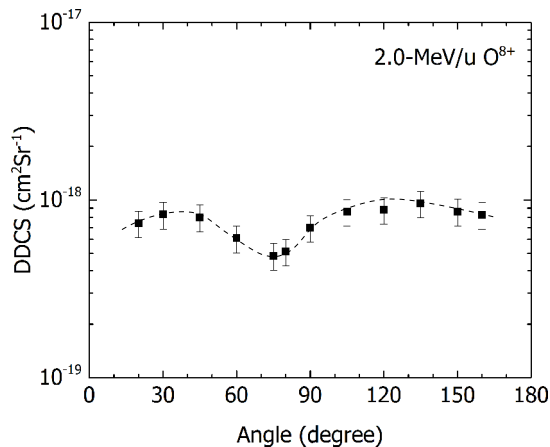
Fig. 7. Oxygen KLL Auger angular distribution for $2.0\,\mathrm{MeV/u}$ O^{8+} projectile. The dashed line is a guide to the eye.

sensitive to the beam energy, charge state as well as non-Coulomb potential, and the molecular wave function. This parameter, however, begins to saturate at a value of ≈ 0.9 for electron energy $>100\,\mathrm{eV}$, as observed for other atomic [31] or molecular targets. The both versions of the CDW-EIS model gave a pretty good agreement with the data. Particularly the post-version gives an excellent account of the asymmetry parameter. However, in the present work, it may not be possible to disentangle different contributions arising from different mechanisms responsible for the asymmetry parameter.

4.4 Single differential cross section

Single differential cross sections $\sigma(\epsilon)$ or $\sigma(\Omega)$ were obtained from our measured double differential cross section results by numerical integration of the DDCS results with respect to electron ejection angle or ejected electron energy. Figure 6 shows a comparison between present experimental measurements and the calculated theoretical SDCS provided by the CDW-EIS model (both prior and post version) while Tables 1 and 2 display the experimentally obtained DDCS and SDCS values. For both the impact energies, a reasonably good agreement can be seen in general with both the theoretical models. In general an overestimation of experimental results by the theoretical calculations can be seen. It is noticed that for the case of $3.75\,\mathrm{MeV/u}$ projectile, agreement with theoretical results are particularly good. The agreement is better in the extreme forward and extreme backward angles. Furthermore, we clearly observe that, the post version of the theory matches better with the experimental results than the prior version.

We have shown the oxygen KLL Auger cross sections (SDCS i.e. derived from the area under KLL-peak) as a function of angle for $2.0\,\mathrm{MeV/u}$ projectile (Fig. 7). An oscillatory structure in the distribution can be seen with a minimum around $75°$. This behavior is in contrast to the distribution observed for the continuum electron DDCS or SDCS for which a peak is observed around this angle. Atomic K-shell vacancies are isotropic and hence Auger decay of these vacancies is also isotropic in absence of
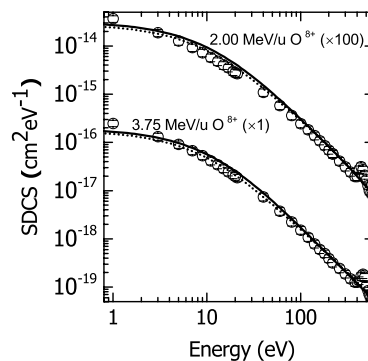
Fig. 8. Single differential cross sections for ejection of electrons by $2.0\,\mathrm{MeV/u}$ and $3.75\,\mathrm{MeV/u}$ O^{8+} ions in collision with waver vapor as a function of the ejected electron energy. The CDW-EIS prior version is shown by the solid line whereas the dotted line represents the CDW-EIS post version. Experimental measurements are represented by circles ($\circ$). For convenience, data and theoretical values for the case of $2.0\,\mathrm{MeV/u}$ O^{8+} has been multiplied by a suitable factor as indicated in the figure.

beam induced alignments. Molecules are different in this respect. They are supposed to exhibit anisotropic behavior arising from the final-state-symmetry, which is very well known [33–35]. In case of heavy-ion induced ionization the additional influence of beam induced alignment causes further angular distribution even in case of atoms, and of course for molecules. The satellite production is also much stronger in case of heavy-ions which is responsible for much stronger anisotropic distribution [31,36,37]. A detailed analysis of the angular distributions of the KLL Auger electrons emitted from molecules, which is beyond the scope of this paper, can be found in references [33,34,36–38]. Although no calculation or a suitable interpretation is available or aimed here, it may be commented that an anisotropic distribution is rather expected.

The single differential cross section as a function of ejected electron energy is shown in Figure 8. Similar to the case of SDCS angular distribution (Fig. 6), here also we can see that the agreement with the theoretical results is better for the case of $3.75\,\mathrm{MeV/u}$ projectile than that for $2.0\,\mathrm{MeV/u}$ projectile.

5 Total ionization cross section

By numerical integration of the SDCS values with respect to angle or energy, total ionization cross section was obtained. The values at the bottom right corner of Tables 1 and 2 represents the TCS values for $2.0\,\mathrm{MeV/u}$ and $3.75\,\mathrm{MeV/u}$ projectiles respectively. Comparison of this TCS value with CDW-EIS models is represented in Table 3. The correction term due to scattering of low energy electrons in gas molecules contributed about 3% in the TCS values.

5.1 TCS-saturation behavior

From the Bethe-Born theoretical model, one expects that TCS $\sim q_p^2 \times \ln E/E$. In order to investigate the projectile

Table 3. Total ionization cross section [present study] (Gb).

Energy (MeV/u)	TCS (experimental)	CDW-EIS (prior)	CDW-EIS (post)
2.00	2.85 ($\pm$0.50)	3.73	3.26
3.75	2.11 ($\pm$0.36)	2.40	2.03
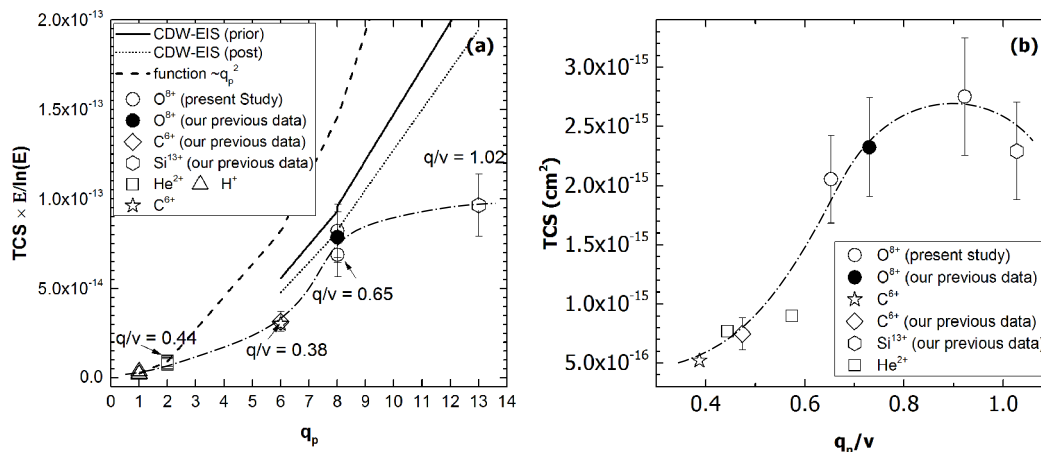
Fig. 9. Scaled total cross sections (TCS $\times E/\ln E$) for different projectiles (p [19,20], He^{2+} [21], C^{6+}[22,23], O^{8+}[24], Si^{13+}[23]) as a function of charge states [plot (a)]. In plot (a), the dashed line represents the first Born predicted q_p^2 dependence, normalized for He^{2+} data. Plot (b) shows the dependence of the total ionization cross section on the Sommerfield parameter (q_p/v). Saturation of TCS values can be seen as q_p/v goes closer to 1. In both the plots, the present data points are denoted by open circles. The CDW-EIS prior and post versions are represented by the solid and dotted lines respectively, indicating a steep rise in the cross sections with q_p in contrast to the almost saturated TCS for higher q_p. In plot (a), the dashed line represents the first Born predicted q_p^2 dependence, normalized for He^{2+} data, while the dash-dotted line is a guide to the eye.

Table 4. Total ionization cross section [available results] (cm^2).

Projectile	Charge state (q_p)	Energy (MeV/u)	TCS
Proton [19,20]	+1	0.1	5.23E$-$16
		0.5	1.30E$-$16
		2	0.44E$-$16
		5	0.36E$-$16
Helium [21]	+2	0.2	1.23E$-$15
		0.3	0.90E$-$15
		0.5	0.77E$-$15
Carbon [22,23]	+6	4	7.22E$-$16
		6	5.22E$-$16
Oxygen [24]	+8	2	2.85E$-$15
		3	2.32E$-$15
		3.75	2.11E$-$15
Silicon [23]	+13	4	2.31E$-$15

q-dependence on the total cross section, TCS $\times E/\ln E$ was plotted as a function of the projectile charge state (q_p) (Fig. 9). The figure shows the scaled TCS (TCS $\times E/\ln E$) for both 2.0 MeV/u and 3.75 MeV/u O^{8+} projectiles along with some other existing TCS results like H$^+$ (taken from [19,20]), He^{2+} (taken from [21]), C^{6+} (taken from [22,23]), O^{8+} (taken from [24] and present study) and Si^{13+} (taken from [23]). These existing TCS results are displayed in Table 4. Our previous data for 4.0 MeV/u C^{6+} and Si^{13+}

projectiles have also been plotted. The first Born predicted q_p^2 dependence has also been plotted (shown by the dashed line in Fig. 9), normalized at He^{2+} projectile data. From the figure, it can be seen that the measured ionization cross section tends to saturate as the projectile charge state (q_p) increases. The deviation from q_p^2 in ion–atom collision has been discussed earlier by various authors (as for example, see [39–46]). This implies that even one increases the charge state the electron

emission does not increase appreciably or show much slower increase compared to that expected according to q_p^2. Although it appears to be surprising we found a similar behavior in case of 1s-excitation and inner shell ionization. For example, a similar kind of saturation behavior for excitation or ionization was previously seen by different authors [47–53]. The 1s electron excitation cross section for He-like Si ions were observed to saturate when plotted against the target atomic number [47]. Tribedi and coworkers [50–52] found the saturation of Ar K-shell ionization cross section as a function of projectile charge state (q_p) (see Fig. 6 in Ref. [50]). The measured L X-ray production cross sections for projectile Cu-ions, arising from the excitation and electron capture process, were also found to saturate as target atomic number increases [54]. Such saturation behavior was explained in terms of Schwinger's variational principle in which the higher-order perturbation effects are included explicitly in the form of a second Born-like term. It was argued that the saturation is caused by the Interplay between the first-order enhancement in the transition amplitude and its dissipation into the system through the coupling among various channels [47]. Such explanation for excitation process can also be found in references [55,56] which used a theory based on the fractional form of the Schwinger variational principle [57]. The present observation only indicates toward a saturation of the ionizations cross sections for higher values of q_p for which the ionization probability increase dramatically and hence the higher order terms much be considered, which in turn produces the saturation behavior due to the cancellation effect, as explained above and in reference [47]. The dependence of the TCS on the perturbation strength i.e. (q_p/v_p) (Sommerfield parameter) is shown in Figure 6b. The TCS reaches a saturation value close to $q_p/v_p=1$. Interestingly it also indicates toward a maximum around the same value of the perturbation strength. It may be necessary to investigate for the data for projectiles other higher charge states (for example $q_p \geq 8$) to prove the saturation effect more convincingly. Such study will also help to establish whether there is a maximum in the distribution i.e. TCS versus perturbation strength.

6 Conclusions

We have reported the absolute double differential cross section (DDCS) of emitted electrons from water-vapor target under the impact of 2.0 MeV/u and 3.75 MeV/u O^{8+} projectile ions. The experimental DDCS results were compared with the CDW-EIS prior and post version model calculations. A reasonably good agreement of the experimental results with the theoretical models were observed for both 2.0 MeV/u and 3.75 MeV/u projectiles. The angular distributions of the lowest energy part (i.e. around 1–20 eV) show a gradual fall which is in contrast to the flat-behavior observed for ion-collisions with multi-electron atom, such as Ne. The DDCS results were integrated to obtain the single differential cross section (SDCS) and total ionization cross section (TCS). The experimental TCS values for 2.0 MeV/u and 3.75 MeV/u

projectiles were 2.85 Gb and 2.11 Gb respectively. The scaled TCS (TCS $\times E/\ln E$) as a function of projectile charge state (q_p) was plotted for both 2.0 MeV/u and 3.75 MeV/u along with some other existing results. The scaled TCS (TCS $\times E/\ln E$) was observed to indicate a saturation behavior with increasing projectile charge state (q_p) in contrast to the steep increase as per the first Born predicted q_p^2 or according to the CDW-EIS prediction. The TCS is shown to indicate a peaking behavior when perturbation strength (q_p/v_p) reaches to unity. This observation is important for the study of electron emission by high projectile ions, in regard to the radiation damage of biological matter. It may be necessary to extend these studies for some other charge state ions with higher perturbation strength for studying the saturation or peaking behavior convincingly.

Author contribution statement

LCT had the idea of the investigation. LCT, SB, CB, MRC conducted the experiment. LCT and SB did all the analysis/interpretation and wrote the paper which was reviewed by all the authors. RDR and JM provided the theoretical calculations.

References

1. J.S. Loeffler, M. Durante, Nat. Rev. Clin. Oncol. **10**, 411 (2013)
2. D. Schardt, T. Elsässer, D. Schulz-Ertner, Rev. Mod. Phys. **82**, 383 (2010)
3. B. Boudaïffa, P. Cloutier, D. Hunting, M.A. Huels, L. Sanche, Science **287**, 1658 (2000)
4. S. Gohlke, A. Rosa, E. Illenberger, F. Brüning, M.A. Huels, J. Chem. Phys. **116**, 10164 (2002)
5. D. Belkić, J. Math. Chem. **47**, 1366 (2010)
6. T. Nakano, M. Suzuki, A. Abe, Y. Suzuki, Cancer J. **5**, 362 (1999)
7. T. Kanai, M. Endo, S. Minohara, N. Miyahara, H. Koyama-Ito, H. Tomura, N. Matsufuji, Y. Futami, A. Fukumura, T. Hiraoka, Y. Furusawa, Int. J. Radiat. Oncol. Biol. Phys. **44**, 201 (1999)
8. M. Jung, H. Rothard, B. Gervais, J.P. Grandin, A. Clouvas, R. Wünsch, Phys. Rev. A **54**, 4153 (1996)
9. H. Rothard, M. Jung, J.P. Grandin, B. Gervais, M. Caron, A. Billebaud, A. Clouvas, R. Wünsch, C. Thierfelder, K.O. Groeneveld, Nucl. Instrum. Methods Phys. Res. B **125**, 35 (1997)
10. H. Rothard, M. Jung, B. Gervais, J.P. Grandin, A. Billebaud, R. Wünsch, Phys. Rev. B **62**, 8818 (2000)
11. G. Schiwietz, G. Xiao, Nucl. Instrum. Methods Phys. Res. B **107**, 113 (1996)
12. P. Bauer, Phys. Res. B **45**, 673 (1990)
13. P. Bauer, F. Kastner, A. Arnau, A. Salin, P.D. Fainstein, V.H. Ponce, P.M. Echenique, Phys. Rev. Lett. **69**, 1137 (1992)
14. J. Tabet, S. Eden, S. Feil, H. Abdoul-Carime, B. Farizon, M. Farizon, S. Ouaskit, T.D. Märk, Phys. Rev. A **82**, 022703 (2010)
15. Y. Iriki, Y. Kikuchi, M. Imai, A. Itoh, Phys. Rev. A **84**, 052719 (2011)

16. A.N. Agnihotri, S. Kasthurirangan, S. Nandi, A. Kumar, M.E. Galassi, R.D. Rivarola, O. Fojón, C. Champion, J. Hanssen, H. Lekadir, P.F. Weck, Phys. Rev. A **85**, 032711 (2012)

17. A.N. Agnihotri, S. Kasthurirangan, S. Nandi, A. Kumar, C. Champion, H. Lekadir, J. Hanssen, P.F. Weck, M.E. Galassi, R.D. Rivarola, O. Fojón, J. Phys. B: At. Mol. Opt. Phys. **46**, 185201 (2013)

18. L.C. Tribedi, A.N. Agnihotri, M.E. Galassi, R.D. Rivarola, C. Champion, Eur. Phys. J. D **66**, 303 (2012)

19. M.A. Bolorizadeh, M.E. Rudd, Phys. Rev. A **33**, 888 (1986)

20. M.E. Rudd, T.V. Goffe, R.D. DuBois, L.H. Toburen, Phys. Rev. A **31**, 492 (1985)

21. L.H. Toburen, W.E. Wilson, R.J. Popowich, Radiat. Res. **82**, 27 (1980)

22. C. Dal Cappello, C. Champion, O. Boudrioua, H. Lekadir, Y. Sato, D. Ohsawa, Nucl. Instrum. Methods Phys. Res. B **267**, 781 (2009)

23. S. Bhattacharjee, S. Biswas, J.M. Monti, R.D. Rivarola, L.C. Tribedi, Phys. Rev. A **96**, 052707 (2017)

24. S. Bhattacharjee, S. Biswas, C. Bagdia, M. Roychowdhury, S. Nandi, D. Misra, J.M. Monti, C.A. Tachino, R.D. Rivarola, C. Champion, L.C. Tribedi, J. Phys. B: At. Mol. Opt. Phys. **49**, 065202 (2016)

25. P.D. Fainstein, G.H. Olivera, R.D. Rivarola, Nucl. Instrum. Methods Phys. Res. B **107**, 19 (1996)

26. C.A. Tachino, J.M. Monti, O.A. Fojón, C. Champion, R.D. Rivarola, J. Phys. B: At. Mol. Opt. Phys. **47**, 035203 (2014)

27. J.M. Monti, O.A. Fojón, J. Hanssen, R.D. Rivarola, J. Phys. B: At. Mol. Opt. Phys. **43**, 205203 (2010)

28. D. Misra, K.V. Thulasiram, W. Fernandes, A.H. Kelkar, U. Kadhane, A. Kumar, Y. Singh, L. Gulyas, L.C. Tribedi, Nucl. Instrum. Methods Phys. Res. B **267**, 157 (2009)

29. Y. Itikawa, N. Mason, J. Phys. Chem. Ref. Data **34**, 1 (2005)

30. F.A. Gianturco, S. Meloni, P. Paioletti, R.R. Lucchese, N. Sanna, J. Chem. Phys. **108**, 4002 (1998)

31. S. Biswas, D. Misra, J.M. Monti, C.A. Tachino, R.D. Rivarola, L.C. Tribedi, Phys. Rev. A **90**, 052714 (2014)

32. P.D. Fainstein, L. Gulyás, F. Martin, A. Salin, Phys. Rev. A **53**, 3243 (1996)

33. O. Hemmers, F. Heiser, J. Eiben, R. Wehlitz, U. Becker, Phys. Rev. Lett. **71**, 987 (1993)

34. D. Dill, J.R. Swanson, S. Wallace, J.L. Dehmer, Phys. Rev. Lett. **45**, 1393 (1980)

35. H. Siegbahn, L. Asplund, P. Kelfve, Chem. Phys. Lett. **35**, 330 (1975)

36. E.G. Berezhko, N.M. Kabachnik, J. Phys. B: At. Mol. Opt. Phys. **10**, 2467 (1977)

37. B. Cleff, W. Mehlhorn, J. Phys. B: At. Mol. Opt. Phys. **7**, 593 (1974)

38. M.H. Prior, R.A. Holt, D. Schneider, K.L. Randall, R. Hutton, Phys. Rev. A **48,** 1964 (1993)

39. K.H. Berkner, W.G. Graham, R.V. Pyle, A.S. Schlachter, J.W. Stearns, R.E. Olson, J. Phys. B: At. Mol. Opt. Phys. **11**, 875 (1978)

40. P. Richard, D.H. Lee, T.J.M. Zouros, J.M. Sanders, J.L. Shinpaugh, J. Phys. B **23**, L213 (1990)

41. D.H. Lee, P. Richard, T.J.M. Zouros, J.M. Sanders, J.L. Shinpaugh, H. Hidmi, Phys. Rev. A **41**, 4816 (1990)

42. A.C.F. Santos, G.M. Sigaud, W.S. Melo, M.M. Sant'Anna, E.C. Montenegro, Phys. Rev. A **82**, 012704 (2010)

43. E.C. Montenegro, G.M. Sigaud, R.D. DuBois, Phys. Rev. A **87**, 012706 (2013)

44. J.L. Shinpaugh, J.M. Sanders, J.M. Hall, D.H. Lee, H. Schmidt-Böcking, T.N. Tipping, T.J.M. Zouros, P. Richard, Phys. Rev. A **45** 2922 (1992)

45. R.E. Olson, K.H. Berkner, W.G. Graham, R.V. Pyle, A.S. Schlachter, J.W. Stearns, Phys. Rev. Lett. **41**, 163 (1978)

46. S. Datz, R. Hippler, L.H. Andersen, P.F. Dittner, H. Knudsen, H.F. Krause, P.D. Miller, P.L. Pepmiller, T. Rosseel, R. Schuch, N. Stolterfoht, Phys. Rev. A **41**, 3559 (1990)

47. U. Tiwari, A.K. Saha, L.C. Tribedi, M.B. Kurup, P.N. Tandon, L. Gulyas, Phys. Rev. A **58**, 4494 (1998)

48. M. Chabot, K. Wohrer, A. Chetioui, J.P. Rozet, A. Touati, D. Vernhet, M.F. Politis, C. Stephan, J.P. Grandin, A. Macias, F. Martin, J. Phys. B: At. Mol. Opt. Phys. **27**, 111 (1994)

49. D. Vernhet, L. Adoui, J.P. Rozet, K. Wohrer, A. Chetioui, A. Cassimi, J.P. Grandin, J.M. Ramillon, M. Cornille, C. Stephan, Phys. Rev. Lett. **79**, 3625 (1997)

50. A. Kumar, D. Misra, A.H. Kelkar, U. Kadhane, Y.P. Singh, G. Lapicki, L. Gulyas, L.C. Tribedi, J. Phys. B: At. Mol. Opt. Phys. **39**, 331 (2005)

51. B.B. Dhal, L.C. Tribedi, U. Tiwari, K.V. Thulasiram, P.N. Tandon, T.G. Lee, C.D. Lin, L. Gulyas, Phys. Rev. A **62**, 022714 (2000)

52. B.B. Dhal, L.C. Tribedi, U. Tiwari, P.N. Tandon, T.G. Lee, C.D. Lin, L. Gulyas, J. Phys. B: At. Mol. Opt. Phys. **33**, 1069 (2000)

53. T. Mukoyama, C.D. Lin, Phys. Lett. A **141**, 138 (1989)

54. A. Kumar, D. Misra, U. Kadhane, A.H. Kelkar, B.B. Dhal, L.C. Tribedi, Radiat. Phys. Chem. **75**, 1704 (2006)

55. B. Brendlé, R. Gayet, J.P. Rozet, K. Wohrer, Phys. Rev. Lett. **54**, 2007 (1985)

56. R. Gayet, M. Bouamoud, Phys. Res. B **42**, 515 (1989)

57. R.G. Newton, *Scattering theory of waves and particles* (Springer Science & Business Media, New York, 2013)